Sensitivity of tropical intraseasonal variability to the pattern of climate warming

Eric D. Maloney[1] and Shang-Ping Xie[2,3]

Received 18 May 2012; revised 28 September 2012; accepted 20 November 2012; published 7 February 2013.

[1] An aquaplanet general circulation model is used to assess the sensitivity of intraseasonal variability to the pattern of sea surface temperature (SST) warming. Three warming patterns are used. Projected SST warming at the end of the 21st century from the Geophysical Fluid Dynamics Laboratory Climate Model 2.1 is one pattern, and zonally symmetric and globally uniform versions of this warming perturbation that have the same global mean SST change are the other two. Changes in intraseasonal variability are sensitive to the pattern of SST warming, with significant decreases in Madden-Julian oscillation (MJO)-timescale precipitation and wind variability for a zonally symmetric warming, and significant increases in MJO precipitation amplitude for a globally uniform warming. The amplitude of the wind variability change does not scale directly with precipitation, but is instead mediated by increased tropical dry static stability associated with SST warming. The patterned SST simulations have a zonal mean SST warming that maximizes on the equator, which fosters increased equatorial boundary layer convergence and also increases equatorial SST relative to the rest of the tropics. Both factors support increased convection, reflected in reduced gross moist stability (GMS). Mean precipitation is decreased and GMS is increased in the off-equatorial Eastern Hemisphere near 10°S in the patterned warming simulations, where the strongest MJO-related intraseasonal precipitation variability is preferred in both the model and observations. It is argued that future changes in MJO activity may be sensitive to the pattern of SST warming, although these results should not be interpreted as a prediction of how MJO activity will change in future climate.

Citation: Maloney, E. D., and S.-P. Xie (2013), Sensitivity of tropical intraseasonal variability to the pattern of climate warming, *J. Adv. Model. Earth Syst.*, *5*, 32–47, doi:10.1029/2012MS000171.

1. Introduction

[2] Scientific research on how the Madden-Julian oscillation (MJO) is anticipated to change with future climate is somewhat limited. *Slingo et al.* [1999] used an index of the band-pass-filtered zonal mean upper tropospheric zonal wind to argue that MJO activity was higher during the mid-1970s to the late 1990s, a time period associated with increased tropical sea surface temperatures (SSTs), than for previous decades. Based on these results, the authors argued that MJO activity would likely increase in the future in association with anthropogenic tropical climate warming. *Jones and Carvalho* [2006] confirmed that an upward linear trend in MJO activity exists in the observational record over the last several decades by examining the amplitude of 850 and 200 hPa MJO zonal wind anomalies. *Pohl and Matthews* [2007], who also found substantial nonstationarity in the relationship between MJO activity and El Nino-Southern Oscillation (ENSO), also confirmed the increase in MJO activity after the mid-1970s. These authors were careful to note that inhomogeneity in the observational record due to increased satellite coverage could affect the interpretation of MJO activity trends, although many of the results derived were supported by complementary modeling work, lending confidence to these conclusions. A relatively larger body of research exists on relationships between MJO activity and ENSO, although no consensus on how overall MJO activity changes with ENSO has yet developed [e.g., *Hendon et al.*, 1999, 2007].

[3] *Jones and Carvalho* [2010] used historical MJO activity to develop a statistical stochastic model based on west Pacific and Indian Ocean warm pool SST for

[1]Department of Atmospheric Science, Colorado State University, Fort Collins, Colorado, USA.
[2]International Pacific Research Center, School of Ocean and Earth Science and Technology, University of Hawaii, Honolulu, Hawaii, USA.
[3]Scripps Institute of Oceanography, University of California, San Diego, California, USA.

1942-2466/13/2012MS000171

predicting the number of MJO events per year. When forced with warming Eastern Hemisphere SSTs from the A1B scenario, the model predicts an increase in the number of MJO events per year at the end of the 21st century, as well as a higher probability of very active MJO years. The model does not account for the change in warm pool SST relative to the tropical mean, which is argued below to be potentially important for determining future MJO activity. It is entirely possible that if other parts of the tropics such as the east Pacific cold tongue region warm more than the Indo-Pacific warm pool, then the Indo-Pacific warm pool SST may decrease relative to the tropical mean [e.g., *Xie et al*., 2010]. This would tend to increase the gross moist stability (GMS) of the Eastern Hemisphere, which has been documented to suppress MJO activity in some previous general circulation model (GCM) experiments [e.g., *Hannah and Maloney*, 2011]. Previous studies have also shown that the MJO is sensitive to other aspects of the mean state of the tropical atmosphere, for example the simulation of basic state low-level westerly flow in the Indo-Pacific warm pool [e.g., *Inness et al*., 2003; *Maloney et al*., 2010]. Changes in the lower tropospheric zonal flow that may occur in association with weakening and or shifts in the tropical circulation may therefore be expected to influence the nature of the MJO in a future climate [e.g., *Vecchi and Soden*, 2007].

[4] *Takahashi et al*. [2011] assessed 12 simulations from the Coupled Model Intercomparison Project Phase 3 (CMIP3) archive to assess how the MJO teleconnection to East Asia will change in the A1B warming scenario. It was shown that seven models exhibited increases in intraseasonal variance over the 21st century, whereas five models demonstrated decreased intraseasonal variance. The models with increased MJO activity demonstrated a warming of the western Indian Ocean and east Pacific corresponding to an SST state that resembled that of a warm ENSO and positive Indian Ocean dipole event. These same models however exhibit consistent present day biases in that their western Indian Oceans SSTs are too warm, and hence MJO activity is too strong in the western Indian Ocean compared to observations. Regardless, these results suggest that MJO activity in the current and future climate is sensitive to basic state SST. *Yoo et al*. [2011] found that a recent trend in frequency of occurrence of particular MJO phases has contributed significantly to trends in high-latitude warming.

[5] The present study uses an aquaplanet GCM that has been previously demonstrated to produce a robust intraseasonal oscillation [e.g., *Maloney et al*., 2010] to explore the issue of how MJO activity may respond to climate change. Recent studies have demonstrated that the projected tropical SST response to global warming is not uniform, and that relatively stronger warming is projected to occur in the equatorial east Pacific and western Indian Ocean compared with other parts of the tropics [e.g., *Xie et al*., 2010], although the precise nature of the warming differs from model to model [e.g., *Zhao and Held*, 2012]. On the other hand, some climate change perturbation experiments described in the literature and available for analysis by the greater community examine the response of the climate system to globally uniform SST perturbations (e.g., Cloud Feedback Model Intercomparison Project, http://cfmip.metoffice.com/, *Bony et al*. [2011]; see also *Cess et al*. [1990]) which may not necessarily produce accurate projections of intraseasonal variability and change. In particular, *Liu* [2013] applied spatially uniform warming perturbations of 2°C and 4°C in an aquaplanet GCM to argue that intraseasonal variability will increase in response to climate warming. We apply different SST warming perturbations to our model, including globally uniform and zonally symmetric patterns and the full projected SST warming pattern from a coupled climate model for the end of the 21st century to assess how MJO activity responds to the pattern of warming. Because our experiments start from an aquaplanet setup that differs in substantial and important ways from the real Earth, we do not make any predictions about how future MJO activity will respond to climate change. To be comfortable in making such predictions, we would need to start from a more realistic basic state SST pattern that is accompanied by as realistic of a simulated MJO as in the model used here. However, our results do suggest that future MJO activity may be sensitive to the pattern of SST warming, which should be taken into account when making projections of future MJO activity.

[6] Section 2 describes the model used in this study and the form of SST perturbations used in the SST warming experiments. Section 3 demonstrates how overall intraseasonal variance and the model intraseasonal oscillation change in response to the different warming patterns. Section 4 presents a process-oriented diagnosis to explain the mean state and intraseasonal variability changes shown in section 3. Section 5 presents conclusions and discussion.

2. Model and Experiment Design

2.1. General Circulation Model

[7] We use a version of the National Center for Atmospheric Research (NCAR) Community Atmosphere Model 3 (CAM3, *Collins et al*. [2006]), in which we have replaced the Zhang-McFarlane convection parameterization with that of relaxed Arakawa-Schubert [*Moorthi and Suarez*, 1992]. This version of CAM3 has been demonstrated to produce superior intraseasonal variability to the standard CAM3, especially with implementation of a minimum entrainment threshold similar to that used in *Tokioka et al*. [1988]. The basic physical configuration of the model is the same as that in the studies of *Maloney et al*. [2010] and *Kiranmayi and Maloney* [2011], which examined the sensitivity of the simulated MJO to the SST basic state. The model is integrated using a spectral core at T42 horizontal resolution, with 26 vertical levels, and a time step of 20 min. Perpetual March 21 insolation is used, although given that we use an uncoupled model the precise insolation distribution has minimal impact on the results.

2.2. SST Basic States

[8] We use a control simulation aquaplanet SST boundary condition that is shown in Figure 1. As

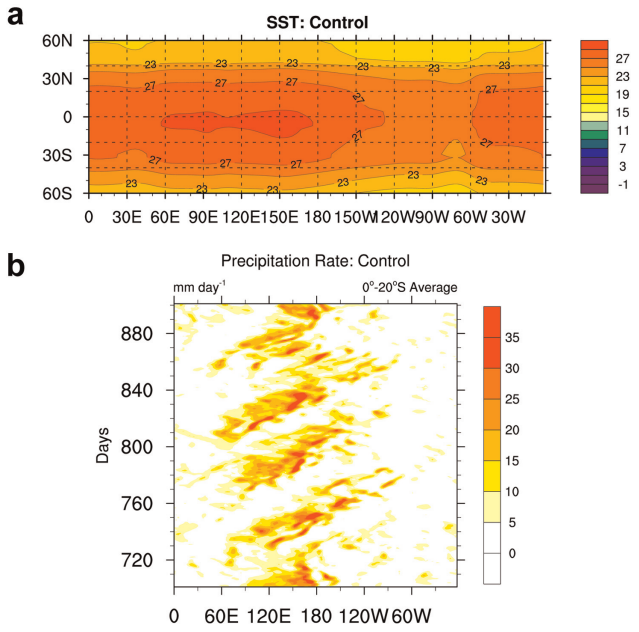

Figure 1. (a) SST distribution for the control simulation and (b) time-longitude diagram of 0°S–20°S averaged precipitation for days 700–900 of the control simulation.

described in *Maloney et al.* [2010], this SST boundary condition was constructed by using an idealized SST distribution based on observations during boreal Spring, but then the SST gradient was reduced to one quarter of that observed poleward of 10°N and 10°S. Although this SST distribution was initially inspired by observations, the modified SST distribution is very different from that of the observed planet. Therefore, SST warming perturbations added to this SST distribution and the resulting MJO activity may not necessarily be expected to mimic the response of the MJO in the real Earth system to climate change, and hence we do not make any claims about the future direction of such changes in MJO activity. However, the results will suggest that changes in MJO activity are highly sensitive to the details of the warming pattern, a conclusion we might expect to have real world relevance.

[9] The control simulation is integrated for 15 years using the SST boundary condition shown in Figure 1. As described in *Maloney et al.* [2010], this simulation produces an extremely robust intraseasonal oscillation that is readily apparent in unfiltered data. A time-longitude diagram of 0°S–20°S averaged precipitation is shown in Figure 1 for one 200 day period of the simulation. Intraseasonal precipitation variability and precipitation anomalies associated with the intraseasonal oscillation in the model maximize in this latitude band (see Figure 4 later). This latitude band is also where observed MJO convection peaks during boreal winter and spring [see *Wheeler and Kiladis*, 1999, Figure 7d]. As is shown later (Figure 6), a well-defined spectral peak in precipitation occurs at 50 day period and zonal wave number 2.

[10] To the control SST distribution in Figure 1, SST warming perturbations are added to represent climate changes. These were generated by using the National Oceanic and Atmospheric Administration (NOAA) Geophysical Fluid Dynamics Laboratory Climate Model 2.1 (CM2.1, *Delworth et al.* [2006]) integrated under the Intergovernmental Panel on Climate Change Special Report on Emissions Warming Scenario A1B [e.g., *Randall et al.*, 2007]. CO_2 concentrations double in this scenario at 2100 and then stabilize. We use the SST change in this scenario as the equilibrium response is approached (the average of the years 2281–2300) relative to the present day as the basis for the SST warming perturbations we use. We do not use the associated trace gas constituent change to force the model as little additional climate change is produced by constituent changes in isolation from the SST influence [e.g., *Allen and Ingram*, 2002; *Deser and Phillips*, 2009]. Figure 2c shows the full patterned CM2.1 SST warming perturbation applied to the model. This was derived using the average January–June SST change in CM2.1 for 2281–2300, which was then interpolated zonally across land. Tropical warming maxima occur between 150°E and 90°W and 30°E and 90°W at longitudes corresponding to the east Pacific cold tongue and western Indian Ocean. The Northern Hemisphere warms more than the Southern Hemisphere. At latitudes where no ocean exists (i.e., Antarctica), SST perturbations were set to those at the closest equatorward latitude.

[11] The equatorial warming peak and preferential Northern Hemisphere warming in Figure 2c are common to many models. For example, *Xie et al.* [2010] showed that this general pattern is produced by both

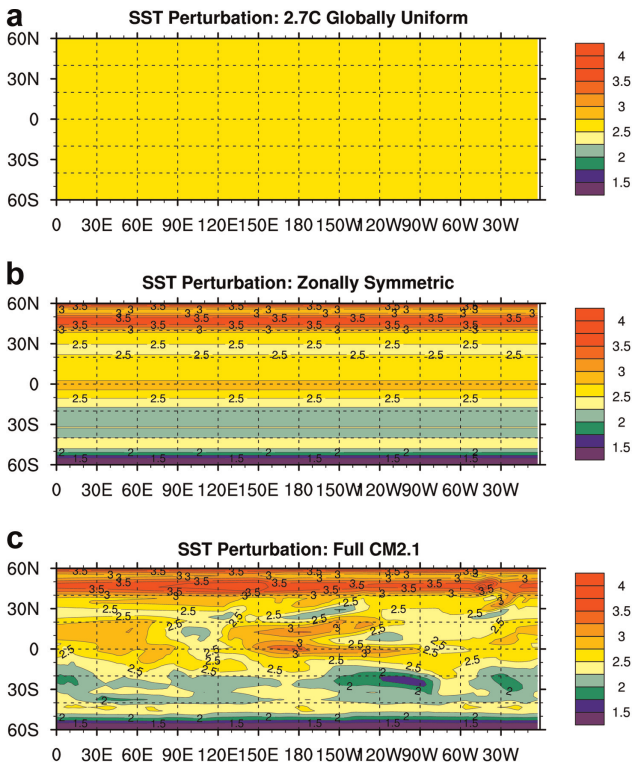

Figure 2. (a) Zonally uniform, (b) zonally symmetric, and (c) full CM2.1 SST perturbations.

the CM2.1 and the NCAR Community Climate System Model 3. This pattern is even apparent in the multimodel mean projections of the CMIP3 models, although the magnitude of the pattern varies significantly from model to model [*Ma and Xie*, 2013]. Given the results shown below, these amplitude variations in the warming pattern may complicate MJO projections in future climate.

[12] In addition to the full CM2.1 SST perturbation, two other perturbation patterns are added to the control SST distribution. These include a perturbation pattern in which the zonal mean of the Figure 2c distribution is applied to all longitudes (Figure 2b), and a globally uniform SST perturbation with the same global mean temperature increase (2.7°C) as the full CM2.1 and zonally symmetric SST perturbations (Figure 2a). The latter distribution is the type of SST perturbation applied in the CFMIP experiments described above, and included as part of the CMIP5 archive. All simulations are integrated for 15 years.

3. Model Mean State and MJO Activity Changes

[13] Figure 3 shows the mean precipitation distribution and the SST boundary condition for the control simulation, and the change in mean precipitation and SST relative to the control simulation for the three

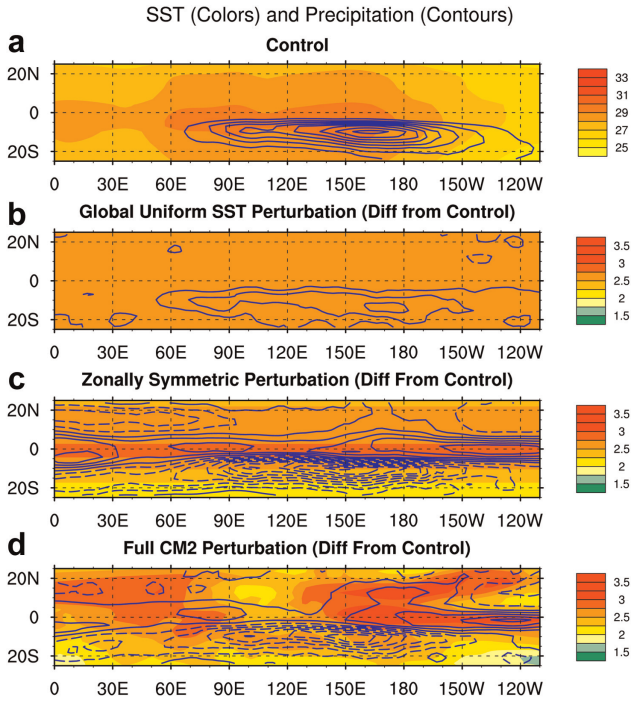

Figure 3. (a) Control SST (colors) and mean precipitation (contours) distributions, and the SST perturbation and precipitation change relative to the control simulation from the (b) globally uniform, (c) zonally symmetric, and (d) full CM2.1 SST perturbations. The contour interval in (a) is 5 mm d^{-1}, starting at 2 mm d^{-1}. The contour interval in (b)–(d) is 1.2 mm d^{-1}, starting at 0.6 mm d^{-1}. Negative contours are dashed.

perturbation experiments. In the control simulation, SST peaks slightly south of the equator, and mean precipitation maximizes at about 10°S in an elongated band on the south edge of the warm pool. The globally uniform warming perturbation creates an increase in precipitation generally collocated with the precipitation maximum in the control simulation. The pattern resembles the "wet-get-wetter" pattern of precipitation change found in previous warming simulations with uniform SST perturbation applied [e.g., *Chou et al.*, 2009; *Xie et al.*, 2010]. No prominent reduction of precipitation occurs at the convective margins, however, as might be associated with the "up-the-ante" mechanism [e.g., *Neelin et al.*, 2003; *Chou et al.*, 2009].

[14] The zonal mean and full CM2.1 warming perturbations generate more substantial changes to the mean precipitation climate, however (Figures 3c and 3d). In both simulations, precipitation is substantially reduced in the region of the control simulation's Southern Hemisphere precipitation maximum, and is substantially increased on the equator. The precipitation increases generally occur in locations where the SST warming is the greatest, with some notable exceptions (e.g., between 30° and 60°E for the full CM2.1 perturbation, Figure 3d). Although SST warms in the Southern Hemisphere tropics in both simulations with patterned warming, mean precipitation is substantially reduced there. The correspondence between the SST pattern change and the mean precipitation change will be explored in more detail below.

[15] Figure 4 shows the mean 850 hPa wind vectors and 20–100 day band-pass-filtered precipitation variance for the control simulation, and the mean wind vectors and the precipitation variance change from the control simulation for the three perturbation experiments. In the control simulation (Figure 4a), intraseasonal precipitation variance maximizes where mean precipitation was shown to be high in Figure 3a. Strong lower tropospheric mean westerlies occur within and to the north of the region of high mean precipitation and precipitation variance. In the uniform warming simulation (Figure 4b), intraseasonal precipitation variance amplifies in place and is significantly higher than that in the control simulation, with slight strengthening of the low-level mean westerly flow. Stippling indicates where precipitation variance is significantly different from that in the control simulation at the 95% confidence level using the chi-square statistic. If one were to use the uniform warming simulation as a proxy for global warming, one would conclude that a significant increase in overall intraseasonal variability occurs in response to global warming, at least when starting from the idealized SST distribution used here. The patterned warming experiments look very different from those of uniform warming. Intraseasonal precipitation variance substantially decreases in the Southern Hemisphere, with significant, but much weaker, precipitation variance increases near the equator. The changes are accompanied by a substantial decrease in the amplitude of mean westerly flow between 60°E and 150°W, which is most strongly pronounced with a zonally symmetric warming perturbation.

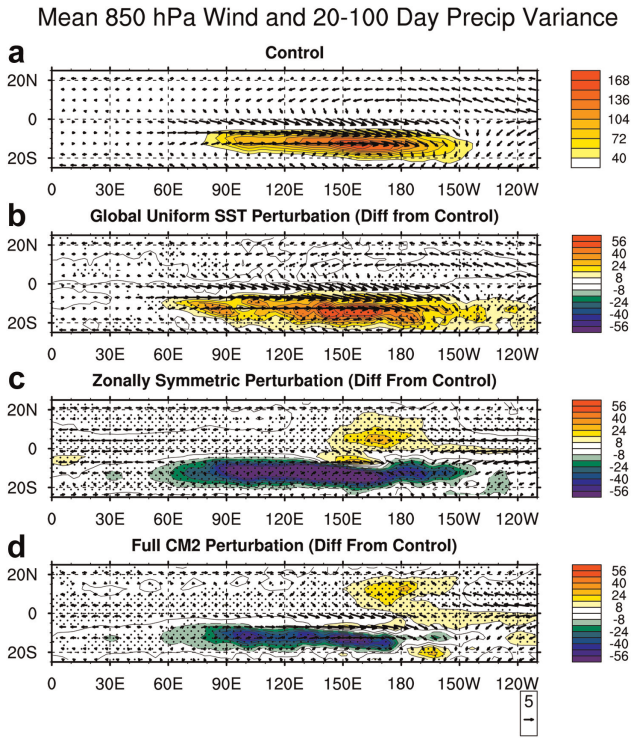

Figure 4. (a) Control mean 850 hPa wind and 20–100 day precipitation variance, and the mean 850hPa wind and the change in 20–100 day precipitation variance relative to the control simulation for the (b) globally uniform, (c) zonally symmetric, and (d) full CM2.1 SST perturbations. Stippling represents where variance is significantly different from the control simulation at the 95% confidence level using a chi-square test. Variance units are in $mm^2\ d^{-2}$.

The corresponding reduction in mean westerlies is interesting, as previous studies have documented a strong relationship between the strength of low-level westerly flow and the strength of the intraseasonal variability simulated by climate models [e.g., *Inness et al.*, 2003]; *Benedict et al.* [2013]. *Maloney et* al. [2010] showed that wind-induced surface flux feedbacks help to destabilize the MJO in the model used here, and that altering the strength of surface mean westerlies would significantly alter the strength of this surface flux feedback, with stronger mean westerlies producing a stronger feedback and hence higher amplitude intraseasonal variability. However, cause and effect is not entirely clear, as stronger intraseasonal variability can also cause stronger mean flow through rectified effects.

[16] Within the region 25°N to 25°S, 0°E to 360°E, the pattern correlations between mean precipitation and the 20–100 day band-pass-filtered precipitation standard deviation changes are 0.95, 0.87, and 0.84 for the uniform warming, zonally symmetric warming, and full CM2.1 warming, respectively. These high correlations indicate that distributions of mean precipitation and precipitation variance are intimately linked, and suggest that processes that force changes in the mean precipitation distribution will also force a change in the distribution of precipitation variance. Such links will be further explored below.

[17] We have also explored whether the local intraseasonal precipitation variability change relative to the control simulation simply scales with the change in mean precipitation. A regression of local mean precipitation change onto the standard deviation of local 20–100 day band-pass-filtered precipitation for all grid cells from 25°S to 25°N indicates a regression coefficient of 1.1 for the uniform warming simulation (where mean precipitation change is the dependent variable). However, the regression coefficients are 1.5 and 1.6 for the realistic and zonally symmetric warming simulations, respectively, indicating deviations from a one-to-one relationship. As mentioned below, MJO-like variability in our model appears to be more strongly fostered when the convective maximum lies slightly off the equator, and hence the nature of the intraseasonal variability in our model appears different depending on where the maximum convective activity is located. Factors in addition to the mean precipitation change thus appear to modulate local intraseasonal variability, although the mean precipitation change appears to be a key factor.

[18] Identical plots to Figure 4, expect for mean 850 hPa wind and 20–100 day band-pass-filtered 850 hPa zonal wind variance, are shown in Figure 5. Significant changes in 850 hPa zonal wind variance do not occur in the uniform warming case, unlike for precipitation variance. Changes in dry static stability in the warming

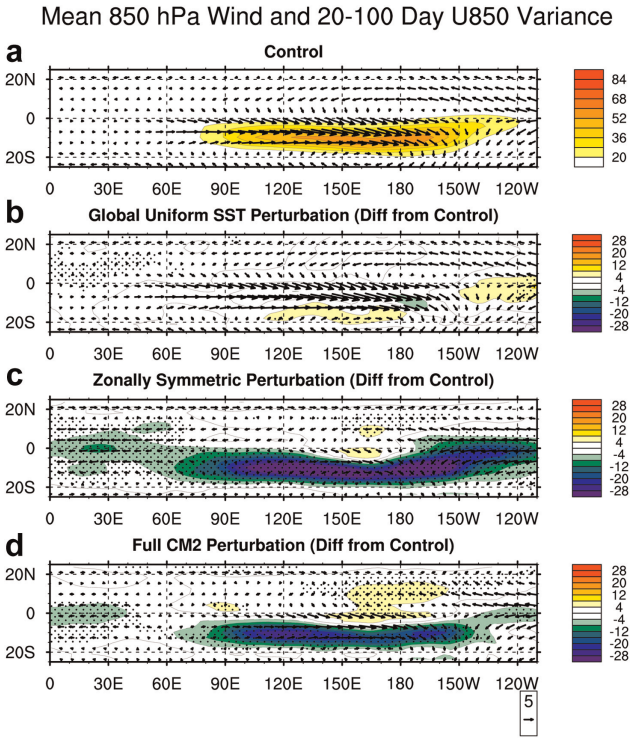

Figure 5. Same as Figure 4, except for 20–100 day 850 hPa wind variance. Variance units are in $m^2\ s^{-2}$.

scenario might explain this potential paradox, as is discussed below. This finding has practical implications for several aspects of climate with future global warming. The MJO has been proposed as an important stochastic forcing mechanism for ENSO, primarily through surface wind stress [e.g., *Moore and Kleeman*, 1999; *McPhaden*, 1999; *Neale et al.*, 2008], and wind anomaly variations associated with the MJO have been documented to affect tropical cyclone activity by impacting vertical wind shear and low-level vorticity [e.g., *Maloney and Hartmann*, 2000; *Molinari and Vollaro*, 2000]. If precipitation variance associated with the MJO increases in a future climate, but wind variability does not, one might expect the practical effects of changes in MJO activity to be more limited in importance.

[19] Intraseasonal wind variance significantly decreases in amplitude across much of the tropics in the zonally symmetric and full CM2.1 warming simulations. Variance decreases maximize to the south of the equator between 60°E and 150°W, although also occur on the equator. Hence, a uniform SST warming pattern produces little significant change in intraseasonal wind variability, but significant decreases in wind variability occur for the cases of patterned warming.

[20] We now assess changes in precipitation and wind variance in the wave number-frequency domain, focusing on the portion of wave number-frequency space explained by the observed MJO. Figure 6 shows space-time spectra of precipitation for the four simulations analyzed here. As described in *Maloney et al.* [2010], the control simulation contains a spectral peak in precipitation centered on 50 days and wave number 2 with amplitude slightly greater than observed. The timescale of the spectral peak does not change among the three

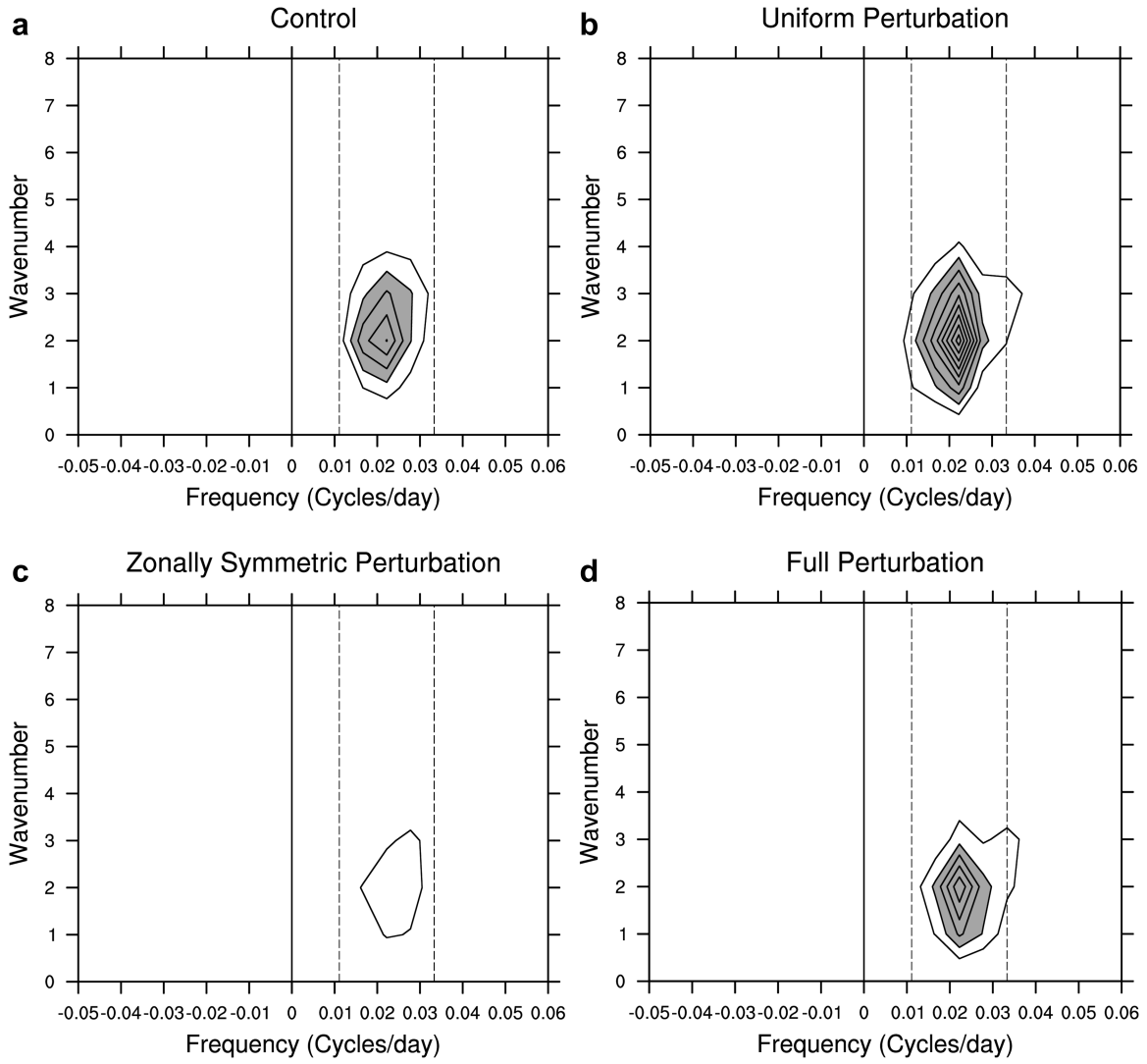

Figure 6. Wave number-frequency spectra of 0°–20°S averaged precipitation during November–April from the (a) control simulation, and for the (b) globally uniform, (c) zonally symmetric, and (d) full CM2.1 SST perturbations. Contour interval is 0.02 $mm^2\ d^{-2}$, starting at 0.04 $mm^2\ d^{-2}$. Values greater than 0.06 $mm^2\ d^{-2}$ are shaded. Spectra are computed on adjacent 180 day segments, and then averaged across realizations to compute an average spectrum.

perturbation experiments and the control, although the spectral peak in the globally uniform warming simulation amplifies relative to the control, the peak in the zonally symmetric simulation is substantially weaker, and that in the full CM2.1 warming simulation appears little changed. The changes in MJO amplitude among the runs will be quantified more precisely below, in addition to changes in zonal wind variance in the MJO band. Regardless, Figure 6 highlights once again the substantial sensitivity of intraseasonal variability to the precise pattern of the warming perturbation applied.

[21] The MJO variance band is defined as the region between eastward zonal wave numbers 1–4, and periods of 30–90 days. Figure 7a shows the ratio of integrated variance in the MJO variance band in the warming perturbation experiments relative to that in the control simulation for precipitation and 850 hPa zonal wind. The spectra were calculated over the latitude band 0°S–20°S. Intraseasonal precipitation and wind variance is still strongly concentrated between 0° and 20°S in all simulations (not shown), even though as shown in Figures 4 and 5 the difference field indicates a reduction in precipitation variance south of the equator relative to the control. In addition to the variance ratio relative to the control, 95% significance bounds on the variance are computed using the chi-square statistic, as shown by the vertical and horizontal lines in Figure 7a. While MJO-band precipitation variance significantly increases in the uniform warming simulation (by 40%), no significant change in precipitation variance occurs with the full CM2.1 warming perturbation. MJO-band precipitation variance decreases by about 60% in the zonally symmetric warming simulation.

[22] The change in 850 hPa zonal wind variance in the MJO band among the three perturbation experiments does not scale like precipitation. While the uniform warming case showed a statistically significant increase in MJO-band precipitation variance, the zonal wind variance only increases by 10%, which is not significant. Likewise, the MJO-band zonal wind variance decreases by 30% in the full CM2.1 warming case, whereas the precipitation variance shows minimal change in the MJO band. Zonal wind variance decreases by 70% in the zonally symmetric warming simulation versus about 40% for precipitation.

[23] Static stability changes may explain the different responses of zonal wind and precipitation variability to warming, consistent with the arguments of *Knutson and Manabe* [1995] and others. *Maloney et al.* [2010] argued that to first order the MJO-like disturbance in the model used here resembles a moisture mode [e.g., *Raymond and Fuchs*, 2009], which is regulated by the weak temperature gradient thermodynamic balance [e.g., *Sobel and Bretherton*, 2000] in which

$$Q' \approx \omega' \frac{\partial \overline{s}}{\partial p}. \quad (1)$$

[24] Here, Q' is the transient apparent heat source, ω' is a vertical velocity anomaly in the MJO disturbance, and $\frac{\partial \overline{s}}{\partial p}$ is the time mean vertical dry static energy gradient, which provides a measure of the static stability. Since diabatic heating anomalies are dominated by convective heating in the MJO convective region, vertically integrated Q' provides to first order the amplitude of precipitation anomalies. Given a basic state static stability, the amplitude of the vertical velocity anomaly required to balance the MJO diabatic heating anomaly can thus be determined.

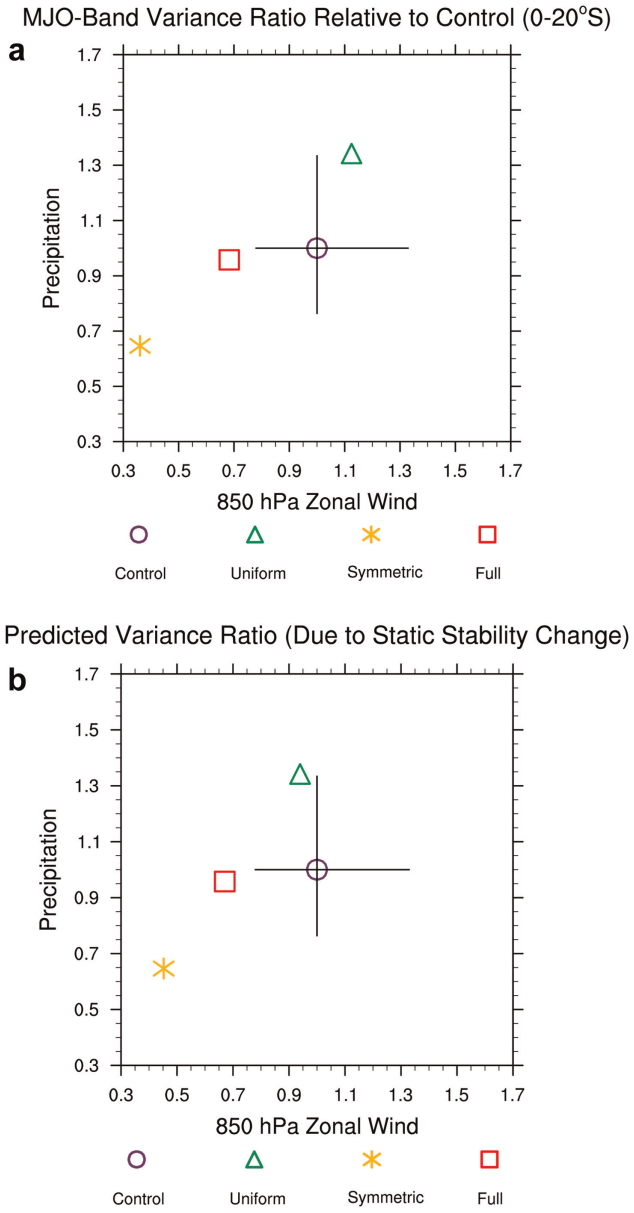

Figure 7. (a) MJO-band variance in precipitation (y axis) and 850 hPa zonal wind (x axis) relative to the control simulation. Black lines represent 95% significance bounds computed using a chi-square test. (b) Precipitation variance relative to the control simulation and the 850 hPa zonal wind variance predicted on the basis of changes in precipitation variance and static stability.

[25] Figure 8 shows the change in vertical profile of potential temperature in the three perturbation experiments relative to the control. The mean vertical velocity

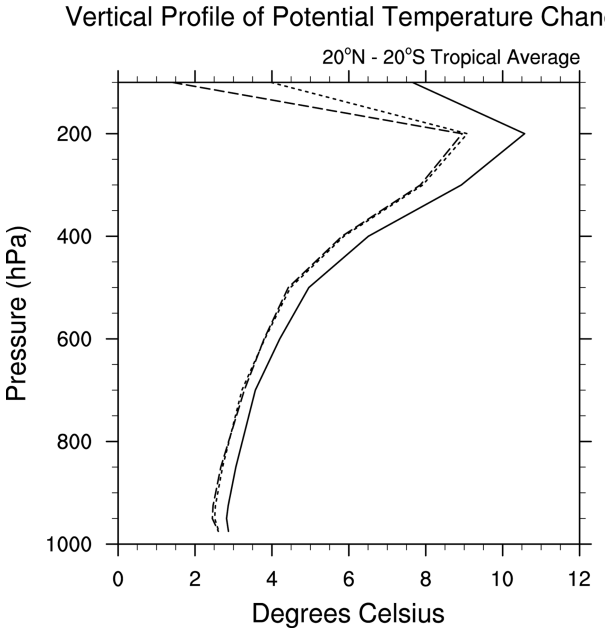

Figure 8. Change in tropics-averaged (20°N–20°S) potential temperature profile relative to the control simulation. The globally uniform simulation is solid, the zonally symmetric case is dashed, and the full CM2.1 perturbation is dotted.

in the region of strongest precipitation variability in the models (Figure 12a), and the perturbation vertical velocity during MJO events in this region (not shown), peak in the middle to upper troposphere, The vertical gradient in potential temperature below 200 mbar indicates increased static stability in the three warming experiments relative to the control. If we do a scale analysis of the perturbation continuity equation for synoptic scale motions, we can show that the characteristic horizontal wind perturbations scale as $U \sim \Omega L/(r\Delta p)$ where Ω is a typical vertical velocity fluctuation, Δp is half the pressure depth of the troposphere (since vertical velocity peaks in the middle troposphere), L is the length scale, and r is the degree of divergence of the flow. If we assume that the degree of divergence of the flow does not change in the warming perturbation experiments, changes to the amplitude of the horizontal flow should scale with the vertical velocity.

[26] Assuming the weak temperature gradient (WTG) balance in (1) holds for model MJO disturbances, we can predict the corresponding zonal wind variance changes relative to the control simulation based on the precipitation variance changes shown in Figure 7a. To this, we use $\frac{\partial \bar{s}}{\partial p}$ at 400 hPa in the four runs to represent static stability (which increases by about 20% at 400 hPa between the control and warming simulations), assume precipitation anomalies are proportional to Q', and then compute the predicted change in wind anomaly amplitude relative to the control using (1). Given the MJO precipitation variance changes, the wind variance changes are predicted reasonably well by changes in static stability (Figure 7b). These include no significant wind variance change in the uniform warming experiment, a 30% decrease in wind variance for the full CM2.1 warming perturbation (whereas precipitation variance did not significantly change), and a nearly 70% decrease in wind variance for the zonally symmetric perturbation. The different responses of the MJO-band wind and precipitation variance changes to warming thus largely appear to be explained by changes in static stability.

4. Process-Oriented Diagnosis

[27] We now conduct a process-oriented diagnosis to determine the reasons for the changes in intraseasonal variability and mean state among the different warming experiments, as these two aspects of the simulations appear to be tightly coupled.

4.1. Tropics-Relative SST and SST-Driven Convergence

[28] We first do an analysis of how local SST relative to the tropical mean SST changes among the warming simulations. Tropics-relative SST has been documented to be a major regulator of tropical convective activity [e.g., *Johnson and Xie*, 2010]. Under the assumption of a simple first baroclinic mode heating profile, negligible horizontal advection, and spatially uniform column-integrated moist static energy (MSE) sources and sinks, *Neelin and Held* [1987] showed that convection should maximize over the regions of warmest tropical SST. A quantity called GMS was developed by *Neelin and Held* [1987], which describes the efficiency at which vertical convective circulations discharge MSE from the column per unit mass flux. Assuming a first baroclinic mode profile, GMS minimizes over warm pool regions, and hence convection needs to maximize there, as it needs to work harder to export column MSE sources. The vertical component of GMS involves the cancellation of two large terms, dry static energy export by divergent circulations (dominant in the upper troposphere) and latent heat convergence that is largest in the lower troposphere. For a fixed vertical velocity profile, dry static energy export is controlled by the tropical mean SST, given the inability of the tropical atmosphere to maintain strong geopotential and temperature gradients [e.g., *Charney*, 1963], whereas lower tropospheric latent heat convergence per unit mass flux is strongly regulated by local SST since lower tropospheric water vapor is strongly constrained by the Clausius-Clapeyron relationship. Hence, under this paradigm, a local increase in SST relative to the tropical mean SST should foster a local increase in convective activity.

[29] Figure 9 shows the tropics-relative SST in the control and three warming simulations. Tropics-relative SST peaks in the Eastern Hemisphere just to the south of the equator in the control simulation. Interestingly, the maximum in mean precipitation is offset to the south and east of the maximum tropics-relative SST. Hence, factors other than GMS may contribute to the location of the precipitation maximum in the control simulation. For example, Figure 15 below shows that surface latent heat flux (column MSE source) peaks to

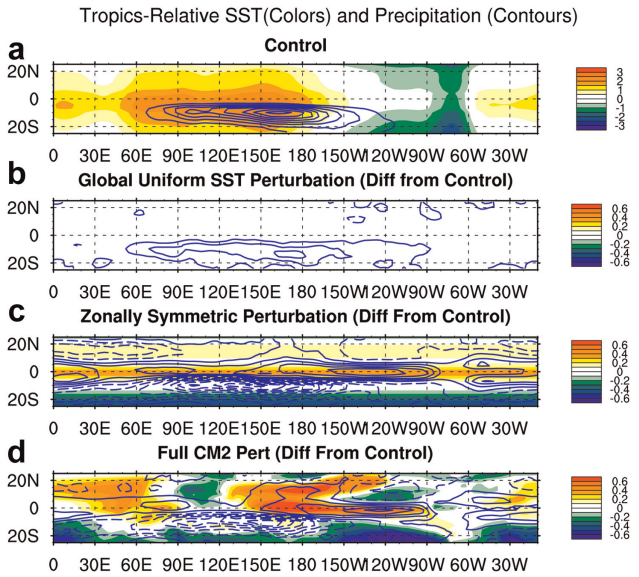

Figure 9. (a) Control simulation local SST relative to the tropical mean SST (colors) and mean precipitation (contours), and the change in tropics-relative SST compared to the control simulation from the (b) globally uniform, (c) zonally symmetric, and (d) full CM2.1 SST perturbations. The contour interval in (a) is 5 mm d^{-1}, starting at 2 mm d^{-1}. The contour interval in (b)–(d) is 1.2 mm d^{-1}, starting at 0.6 mm d^{-1}. Negative contours are dashed.

the south of the maximum tropics-relative SST, which may contribute to the slight displacement of the precipitation maximum. Regardless, we now examine how local changes in tropics relative SST in the warming experiments compare to the control, and relate these to mean precipitation changes. Obviously, the uniform warming simulation does not exhibit a change in tropics-relative SST compared to the control (Figure 9b). However, the patterned warming runs do, and mean precipitation changes in the tropics appear to broadly follow these changes in tropics-relative SST (Figures 9c and 9d). In particular, both tropics-relative SST and mean precipitation increase on the equator and decrease south of 5°S in the patterned perturbation experiments. In the full CM2.1 perturbation experiment, increases in relative SST and precipitation maximize near the equator from 150°E to 90°W. Pattern correlations (20°S–20°N) between the tropics-relative SST change and the mean precipitation change are 0.6 and 0.4 for the zonally symmetric and full CM2.1 warming perturbations, respectively. Hence, the tropics-relative SST change explains a substantial portion of the variance of the mean precipitation change, but not all.

[30] Because equatorial SST is enhanced in the patterned warming simulations relative to the control, we might also expect the possibility that SST gradient-driven convergence helps to focus precipitation there [e.g., *Lindzen and Nigam*, 1987; *Back and Bretherton*, 2009]. As in *Back and Bretherton* [2009], we use the bulk mixed layer model of *Stevens et al.* [2002] to simulate the boundary layer flow. To do so, we first estimate a boundary layer temperature by assuming that the temperature falls off linearly from the SST to a mean 850hPa temperature, thus tying horizontal boundary layer temperature variations to SST. As in *Back and Bretherton* [2009] and *Lindzen and Nigam* [1987], density is determined by linearization about a mean temperature (in this case, we use 288 K). Then, hydrostatic balance is used to determine the surface pressure by integrating downward from the 850 hPa pressure surface. The bulk boundary layer flow due only to the SST-driven pressure perturbation can then be determined in the following way [*Stevens et al.*, 2002; *Back and Bretherton*, 2009]:

$$U = \frac{-(f\partial P_s/\partial y + \varepsilon \partial P_s/\partial x)}{\rho_o(\varepsilon^2 + f^2)}, \tag{2}$$

$$V = \frac{(f\partial P_s/\partial x - \varepsilon \partial P_s/\partial y)}{\rho_o(\varepsilon^2 + f^2)}. \tag{3}$$

[31] Here, ε is a coefficient of mixing and entrainment prescribed to be 1.5×10^{-5} s^{-1}, which is in the range of values suggested by *Back and Bretherton* [2009], although this number is only weakly constrained by observations. ρ_o is a reference boundary layer density that we set to 1.225 kg m^{-3}, P_s is the surface pressure, and f is the Coriolis parameter.

[32] Figure 10 shows the change in zonal mean SST-driven boundary layer convergence relative to the

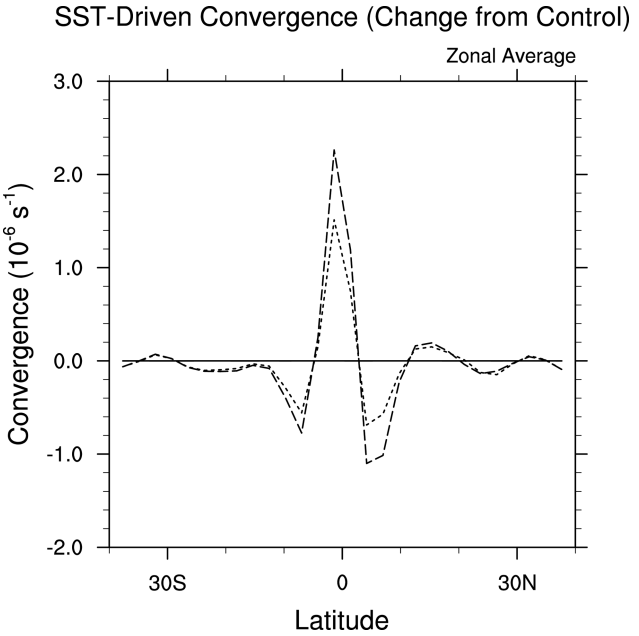

Figure 10. Difference in zonal mean boundary layer model SST-driven convergence compared to the control for the (solid) globally uniform, (dashed) zonally symmetric, and (dotted) full CM2.1 warming simulations.

control derived from (2) and (3) for the three warming simulations. The SST-driven convergence distribution for the control simulation is nearly identical to that in the uniform warming case. In the patterned warming simulations, equatorial SST-driven convergence is increased relative to the uniform warming simulation. The SST-driven convergence maximum in the uniform warming simulation occurs poleward of the convergence center in the patterned warming cases (not shown). Equatorial SST-driven convergence increases by greater than a factor of 3 for the zonally symmetric warming run as compared to the control and uniform warming simulations (not shown). More modest amplitude increases in SST-driven off-equatorial divergence (centered at 7.5°S and 5°N) occur in the patterned warming cases relative to the control.

[33] Figure 11a shows the actual change in boundary layer convergence (using negative one times 850 hPa omega divided by 150 hPa as a proxy) in the three warming cases relative to the control. Although convergence changes in the uniform warming case are relatively modest, convergence changes in the patterned warming cases are more substantial, with the equatorial increases in convergence reasonably explained in magnitude by the SST-driven convergence field shown in Figure 10. While off-equatorial SST-driven divergence increases also occur in the patterned warming cases (Figure 10), these divergence maxima are displaced in latitude relative to the actual divergence changes shown in Figure 11, but can explain some of the pattern. Figure 11b also shows the change in zonal mean precipitation for the three warming simulations relative to the control. Equatorial increases in SST-driven convergence accompany precipitation increases in the patterned warming runs, and may also contribute to off-equatorial divergence and suppression of precipitation, particularly in the Southern Hemisphere. Maybe not surprisingly, precipitation reductions are greatest in the Southern Hemisphere in the patterned warming simulations, which is consistent with previous studies showing that the tropical precipitation maximum tends to shift toward the hemisphere in which the extratropical heating perturbation is greatest [e.g., *Broccoli et al.*, 2006; *Kang et al.*, 2008]. Figure 2 shows that the patterned warming simulations imply an increased Northern Hemisphere extratropical heating, which is consistent with the asymmetric precipitation changes.

[34] Changes in vertical velocity profiles along the equator in the Western Hemisphere in the patterned warming simulations are consistent with an increase in SST-driven convergence. Figure 12 shows mean pressure velocity profiles in all simulations for a location near the warm pool convective maximum (10°S, 127°E) and along the equator in the Western Hemisphere near the precipitation change maximum shown in Figure 3 (1°N, 242°E). Similar to that shown in *Back and Bretherton* [2006] for the east Pacific Intertropical Convergence Zone (ITCZ) on the real Earth, the region of prominent SST-driven convergence in the Western Hemisphere in the patterned warming simulations is accompanied by a bottom-heavy maximum in vertical velocity

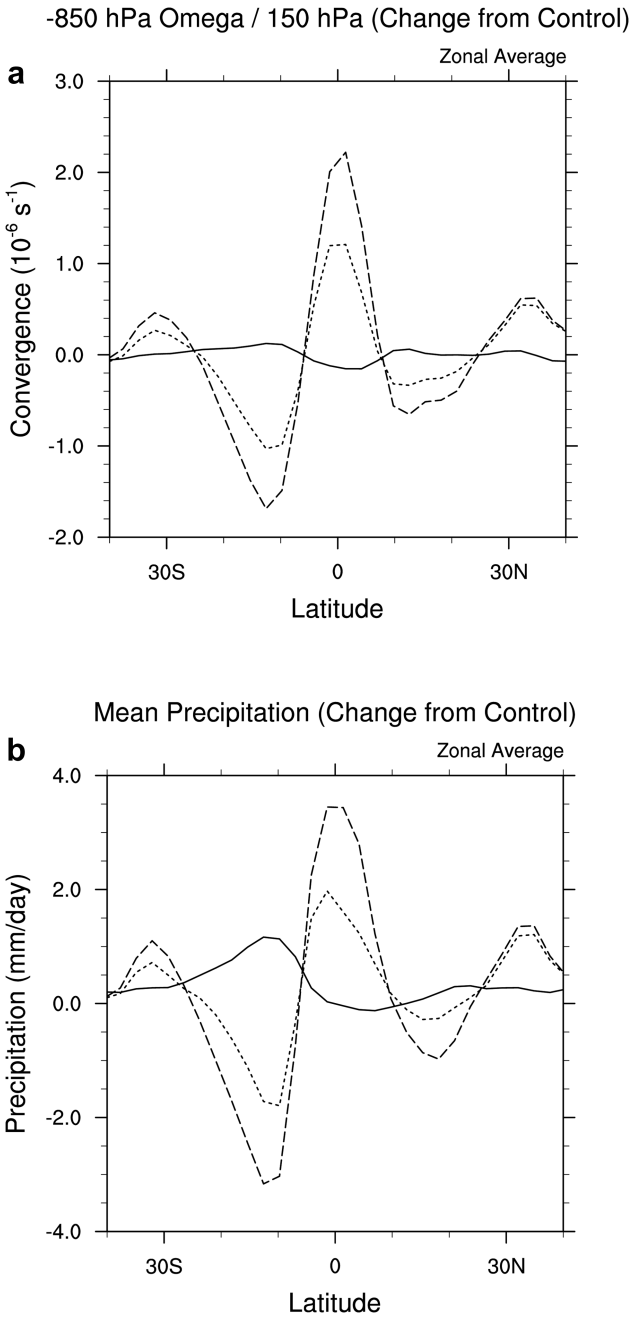

Figure 11. (a) Actual zonal mean boundary layer convergence change compared to the control for the (solid) globally uniform, (dashed) zonally symmetric, and (dotted) full CM2.1 warming simulations, and (b) the change in zonal mean precipitation relative to the control for the (solid) globally uniform, (dashed) zonally symmetric, and (dotted) full CM2.1 warming simulations.

(Figure 12b). The modeled Eastern Hemisphere warm pool region (Figure 12a) shows a top-heavy heating profile. These results support the importance of SST-induced boundary layer convergence for supporting equatorial convection in the patterned warming runs, apparently at the expense of convection off the equator.

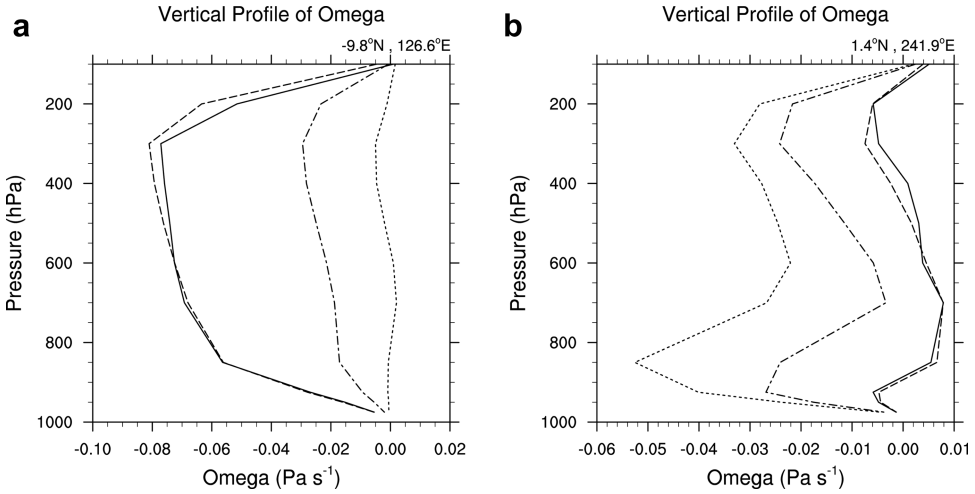

Figure 12. Vertical profiles of omega for (a) off-equatorial Eastern Hemisphere and (b) equatorial Western Hemisphere locations. The control simulation is solid, the globally uniform perturbation simulation is dashed, the zonally symmetric perturbation simulation is dotted, and the full CM2.1 perturbation simulation is dot dashed.

4.2. MSE Export

[35] We now explicitly examine the tropical MSE budget to clarify the importance of tropics-relative SST and SST-driven convergence changes shown above to changes in mean precipitation and its variability. The tropical MSE budget is a powerful tool for understanding where convection is favored and how convection acts to modify the MSE of its environment. As in *Maloney* [2009], the column-integrated MSE budget can be written as follows:

$$\left\langle \frac{\partial h}{\partial t} \right\rangle + \left\langle \omega \frac{\partial h}{\partial p} \right\rangle + \langle \vec{v} \cdot \nabla h \rangle = \mathrm{LH} + \mathrm{SH} - R, \qquad (4)$$

where h is the MSE, $\vec{v}$ is the horizontal wind vector, LH and SH are the surface latent and sensible heat fluxes, and R is the column-integrated radiative cooling. Brackets represent a vertical integral over the depth of the troposphere, here defined to have a top at 100 hPa. Rearranging and using the WTG approximation (i.e., $\frac{\partial T}{\partial t} = 0$), (4) can be written as

$$\left\langle L \frac{\partial q}{\partial t} \right\rangle = \Gamma_v \langle \nabla \cdot (\vec{v} q) \rangle + \Gamma_h \langle \nabla \cdot (\vec{v} q) \rangle + \mathrm{LH} + \mathrm{SH} + R. \qquad (5)$$

[36] As in *Raymond et al.* [2009], the normalized vertical component of GMS is defined as

$$\Gamma_v = -\frac{\langle \omega \partial h / \partial p \rangle}{\nabla \cdot (\vec{v} q)}, \qquad (6)$$

where q is the specific humidity. This quantity represents MSE export by vertical advection per unit convective activity. Here, we represent convective activity by moisture convergence. Similarly, the horizontal component of GMS is defined as

$$\Gamma_h = \frac{-\langle u \partial h / \partial x + v \partial h / \partial y \rangle}{\langle \nabla \cdot (\vec{v} q) \rangle}, \qquad (7)$$

and represents the MSE export by horizontal advection per unit convective activity. As in *Raymond et al.* [2009], smoothing in time was applied separately to the numerator and denominators of (6) and (7) before calculating Γ_v and Γ_h. We do this by applying a running 10 day mean. To ensure that the denominators of (6) and (7) do not go to zero, data are set to missing where the magnitude of the vertically integrated latent heat convergence falls below 5 W m^{-2}.

[37] GMS is a diagnostic that gives a measure of how efficiently convection and associated large-scale motions export MSE from the column. Under WTG balance [e.g., *Sobel and Bretherton*, 2000], this is equivalent to the efficiency in which convection discharges moisture from the column per unit convective activity, as shown by (5). Because of the dominant balance in WTG (a form of which is shown in (1)), the numerator of Γ_v (6) includes the implicit cancellation of condensation due to precipitation processes and vertical moisture advection. We may expect that areas where GMS is low would support increased convection, because in these regions, convection needs to work harder to remove sources of moist entropy (i.e., the sum of terms on the right side of (4)) from the column. In other words, convection is less effective at drying the column in these regions. Neglecting spatial variations of the source terms on the right side of (4), GMS variations help us to diagnose where in the tropics conditions are most favorable for convection [*Neelin and Held*, 1987]. In region of shallow convection where low-level moisture convergence is greater than the condensational moisture loss, GMS can even be negative, reflecting that

the direct actions of convection moisten the column. Our diagnosis of GMS will help confirm the critical roles for increases in SST-driven boundary layer convergence and tropics-relative SST for causing increased equatorial convection in the patterned warming simulations, which in the previous sections was left as speculative.

[38] Figure 13a shows the zonal mean distribution of Γ_v for the three warming simulations. The control distribution of Γ_v looks similar to that of the uniform warming perturbation and therefore not shown. While GMS is a noisy quantity, Figure 13a shows that zonal mean Γ_v is a minimum near 10°S in the uniform warming simulation, consistent with latitudes of maximum mean and variability of precipitation shown in Figures 3a and 4a, respectively. The lowest values of Γ_v occur at longitudes of 150°E–180°E (not shown). However, in the patterned perturbation simulations, Γ_v is a minimum near the equator and actually turns negative in the zonally symmetric perturbation experiment. The negative Γ_v is consistent with the bottom-heavy vertical velocity profile shown in Figure 12 in the region of enhanced SST-driven convergence, which is also observed in the east Pacific ITCZ of the real Earth [*Back and Bretherton*, 2006]. For the patterned warming, this minimum in Γ_v near the equator supports enhanced convection there.

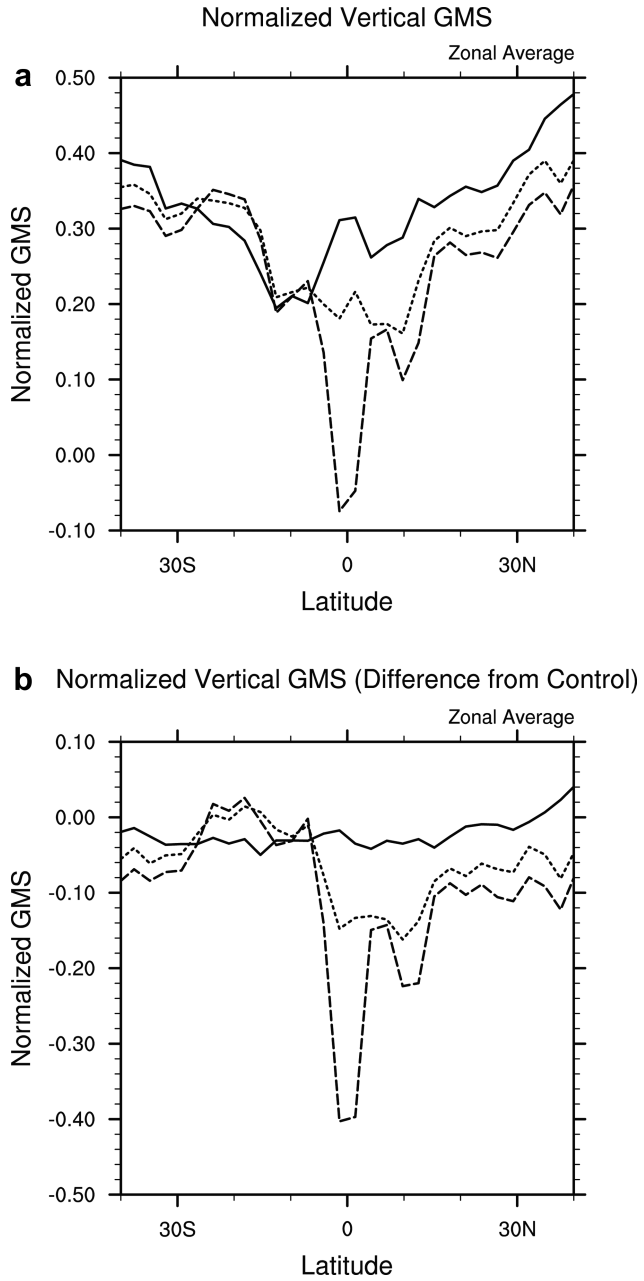

Figure 13. Zonal mean normalized vertical component of GMS for the (solid) globally uniform, (dashed) zonally symmetric, and (dotted) full CM2.1 warming simulations, and (b) the same as (a), except for the change relative to the control simulation.

[39] Figure 13b shows differences in Γ_v from the control simulation. Changes in Γ_v south of the equator in the zonal mean are subtle in all warming simulations, although the patterned warming perturbations both indicate an increase in Γ_v of 0.1 averaged over the region 0°S–20°S, 90°E–180°E relative to the control (not shown), which corresponds to the region of maximum intraseasonal precipitation variance in the control simulation (Figure 4). By making modifications to moist physics in a version of the GCM used here with full continental configurations, *Hannah and Maloney* [2011] demonstrated that increases in Γ_v of such magnitude are associated with changes in the simulation of intraseasonal variability between a state with exceedingly weak intraseasonal variability to one with realistic amplitude. Figure 13b indicates prominent decreases in zonal mean equatorial Γ_v for the patterned warming simulations, with the zonally symmetric simulation exhibiting changes in the zonal mean of -0.4. These changes reflect conditions more favorable for convection on the equator, which is consistent with the precipitation increases seen in Figure 11b. This reduction of Γ_v on the equator is consistent with the increase in SST-driven convergence and tropics-relative SST there, as discussed in section 4.1.

[40] Figure 14 shows the corresponding zonal mean Γ_h and the change in zonal mean Γ_h relative to the control simulation. Γ_h goes up on the equator in the patterned warming simulations to compensate for substantial decreases in Γ_v. This tendency is consistent with the GCM experiments of *Hannah and Maloney* [2011] described above, and also what is observed in nature in the region of the east Pacific ITCZ, where diabatic heating profiles are shallow and SST-driven convergence is prominent that leads to small or negative Γ_v, but compensating larger values of Γ_h [*Back and Bretherton*, 2006]. Our interpretation is that more vigorous convective disturbances and associated large-scale circulations are fostered on the equator associated with low or negative Γ_v. This increased activity enhances horizontal advection of dry, colder air from higher latitudes. Previous observational studies and modeling results have shown that transient disturbances such as easterly waves can act to enhance horizontal advection [e.g., *Peters et al.*, 2008; *Maloney*, 2009; *Hannah and Maloney*, 2011; *Andersen and Kuang*, 2012].

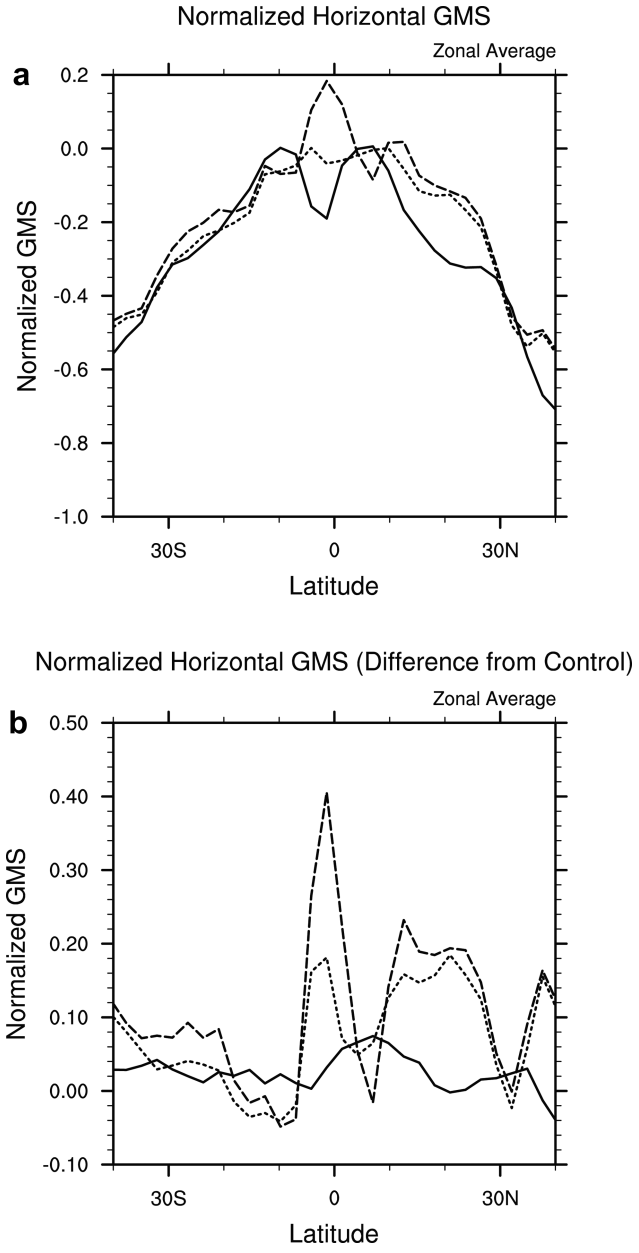

Figure 14. Same as Figure 13, except for the normalized horizontal component of GMS.

[41] In the absence of changes in column moist entropy sources and sinks, we might expect the GMS changes described above to be sufficient to diagnose changes in convective activity in the tropics in the warming simulations [e.g., *Neelin and Held*, 1987]. However, the change in mean lower tropospheric wind vectors in Figure 4 indicates a reorganization of the large-scale atmospheric circulation in the patterned warming simulations such that mean westerlies between 60°E and 150°W are significantly weakened, and mean low-level easterlies elsewhere are strengthened. These changes in mean wind vector amplitude correspond to a decrease in mean surface wind speed in westerly regions, and increase of mean wind speed in easterly regions (not shown), which can modulate the amplitude of surface fluxes. Further, SST increases would tend to increase the surface latent heat flux in the presence of constant boundary layer relative humidity, with these effects greatest over the areas of largest SST change. Figure 15 shows the mean surface latent heat flux for the control simulation and the change in mean latent heat flux for the three warming simulations. The uniform warming simulation exhibits modest increases in latent heat flux across many areas of the tropics, but the patterned warming simulations demonstrate more substantial mean latent heat flux changes, with decreases of up to 60 W m^{-2} in the Southern Hemisphere between 60°E and 180°E in the zonally symmetric warming simulation, and more modest increases in other parts of the tropics. Changes in flux are due to both wind-driven and thermodynamic factors.

[42] To provide an estimate of whether the reorganization of tropical latent heat fluxes may substantially influence the precipitation distribution in the context of the GMS changes described above, we do an analysis of normalized latent heat flux. The normalized MSE export due to local surface latent heat flux is given by $LH/\langle\nabla\cdot(\vec{v}q)\rangle$, which can effectively be used to rewrite the LH term in (5) in the same form as for vertical and horizontal MSE advection. We calculate the mean moisture convergence and latent heat flux separately

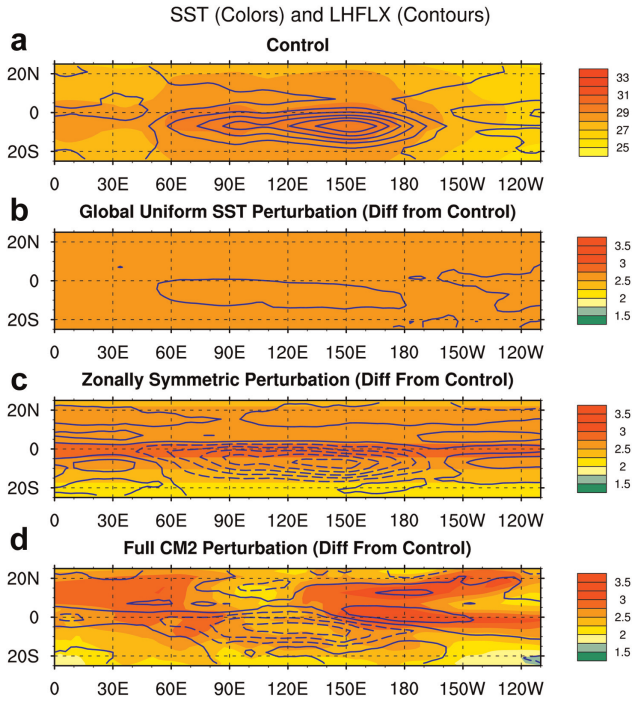

Figure 15. (a) Control SST (colors) and mean latent heat flux (contours) distributions, and the SST perturbation and latent heat flux change relative to the control simulation for the (b) globally uniform, (c) zonally symmetric, and (d) full CM2.1 SST perturbations. The contour interval in (a) is 20 W m^{-2}, starting at 50 W m^{-2}. The contour interval in (b)–(d) is 12 W m^{-2}, starting at zero. Negative contours are dashed.

for each run and then analyze the term $\Delta LH/\langle\nabla\cdot(\vec{v}q)\rangle$, where ΔLH is the change in the latent heat flux relative to the control simulation, and $-\langle\nabla\cdot(\vec{v}q)\rangle$ is the mean moisture convergence of the control simulation. The normalized latent heat flux export due solely to the change in latent heat flux increases by 0.1 to 0.2 in the center of the region of maximum warm pool precipitation in Figure 3a for the patterned warming runs (not shown), which is of the same order of magnitude as the increase in the vertical component of GMS there. Therefore, the reorganization of the latent heat flux distribution appears comparably important as the change in GMS to the MSE budget. This should only be considered a rough analysis, however, as the change in the vertically integrated moisture convergence from the control to patterned warming cases is not small.

4.3. Discussion

[43] We have shown above that patterned warming simulations exhibit a decrease in MJO-like variability, and that these decreases are associated with mean state changes such that equatorial precipitation is enhanced and off-equatorial precipitation and intraseasonal variability shows substantial decreases. However, it has not been conclusively argued why such changes should diminish the amplitude of the MJO in the model. We first provide some discussion of this point here.

[44] It was shown in *Maloney et al.* [2010] that the MJO in the model used here resembles a "moisture mode", a tropical disturbance regulated by WTG theory, in which the processes that regulate the moisture budget are fundamental to understanding the destabilization and the propagation of the disturbance [e.g., *Raymond*, 2001]. As shown by *Raymond* [2001] for a flat SST distribution, all else being equal the convective anomalies of an MJO-like moisture mode prefer to lie off the equator, as moisture modes are balanced disturbances in which the low-level flow is highly rotational. *Maloney et al.* [2010] showed that convective anomalies associated with the MJO-like disturbance in the control simulation tend to maximize at 10°S, and hence increasing the GMS at those latitudes, as occurs in the patterned warming perturbations above, would tend to weaken the amplitude of the MJO-like disturbance. We also note from *Wheeler and Kiladis* [1999] that 10°S is approximately where MJO-band convective variance maximizes during boreal winter and spring (see their Figure 7).

[45] We cannot rule out other changes to the basic state of the model caused by the patterned SST warming are responsible for the change in MJO activity. For example, we showed in Figure 4 that regions of mean low-level westerlies appear to weaken in the patterned warming simulation, and regions of mean low-level easterlies strengthen. Increases in mean precipitation in the patterned warming simulations largely occur in regions of strengthened mean easterlies (compare Figures 3 and 4). Basic state westerlies produce the correct phasing between surface latent heat flux anomalies and precipitation anomalies in intraseasonal disturbances, which appears necessary to destabilize the MJO in our model [*Maloney et al.*, 2010]. These results are supported by the aquaplanet results of *Kiranmayi and Maloney* [2011], who showed in the same GCM used here that a zonally symmetric SST distribution with mean easterlies everywhere across the tropics produces only weak intraseasonal variability. Similarly, weakening but not reversing the mean westerlies would weaken the surface flux feedback and lead to lower MJO amplitude. This result may be somewhat model dependent [e.g., *Andersen and Kuang*, 2012], although at the least in the model we use mean westerlies appear necessary to destabilize the MJO.

[46] Although this study was conducted using an SST basic state that is highly idealized with a meridional SST gradient a quarter of that observed, we also conducted warming perturbation experiments in which the meridional SST gradient was not reduced to a quarter of that observed, and hence more realistic. The control simulation MJO with this modified SST distribution is not as realistic as described above (e.g., Figure 6a), and has dominant precipitation variance centered near 100 day period (not shown). However, we still assessed the change in amplitude of this mode for different climate warming patterns. Doing a similar analysis as in Figure 7a, a significant increase in precipitation amplitude occurs for a uniform warming perturbation, and a significant decrease in wind amplitude occurs for the zonally symmetric warming (not shown). Other changes from the results presented here are not significant. These results support our basic conclusion that changes in future MJO activity are sensitive to the pattern of SST warming.

[47] These conclusions should be contrasted with those such as *Liu* [2013] that use a uniform SST warming to assess the change in MJO activity in future climate. *Liu* [2013] found a general increase in intraseasonal variability and the frequency of MJO events with 2°C and 4°C uniform warming perturbations, with the greatest increases occurring at 20–30 day timescale. Our results suggest that caution should be used when interpreting such results, since patterned SST warming as is projected by coupled climate models may produce a different response.

5. Conclusions

[48] An aquaplanet GCM with a robust MJO-like disturbance was used to assess the sensitivity of the model MJO simulation to the pattern of SST warming. The near-equilibrium SST warming (interpolated across land) in the Intergovernmental Panel on Climate Change (IPCC) A1B scenario in the GFDL CM2.1 model was used as the base SST perturbation. The zonal mean of this pattern, as well as a uniform warming field derived from the global average of the base perturbation field, were also used to perturb the aquaplanet model. Hence, in all simulations, the global mean temperature perturbation is 2.7°C, although with different warming patterns. The full CM2.1 warming case and the zonally symmetric warming case have a local maximum in zonal mean SST change on the equator.

[49] Results show that the amplitude and sign of the changes in MJO activity and the distribution of tropical

intraseasonal variance are sensitive to the pattern of SST warming. Application of a globally uniform warming enhances the amplitude of precipitation variance in the MJO band, although the amplitude of wind variability is not significantly changed. A zonally symmetric warming produces statistically significant reductions in both MJO wind and precipitation variance. The full CM2.1 warming simulation exhibits substantial reductions in MJO wind variance, with modest reductions in precipitation variance. The different amplitudes of MJO precipitation and wind variance changes across simulations can be explained to first order by increases in tropical dry static stability associated with SST warming.

[50] Changes in tropical variability in different warming scenarios are intimately coupled to changes in the model mean state. For example, the spatial pattern correlations between tropical intraseasonal precipitation variability changes and mean precipitation changes are 0.84 or greater for all simulations. Given such links, the processes responsible for changes in the mean state and related changes in model variability were examined. It was shown that SST relative to the tropical mean SST, as well as SST gradient-driven boundary layer convergence, increase on the equator in the patterned warming cases. The SST-driven convergence is associated with a relatively shallow vertical velocity maximum as observed in the east Pacific ITCZ region in observations [e.g., *Back and Bretherton*, 2009]. Both of these factors tend to decrease GMS on the equator, which indicates that conditions are more favorable for convection there. These reductions in GMS were verified by explicit calculations using the MSE budget. Significant increases in GMS off the equator in the patterned warming runs are consistent with the decreases in MJO activity seen in these simulations, as the model MJO convective center prefers to lie off the equator. The MJO in the model resembles a moisture mode [e.g., *Raymond and Fuchs*, 2009], with a convective maximum preferring to exist about 10° of latitude off the equator, not unlike that shown in observations [e.g., *Wheeler and Kiladis*, 1999]. Hence, changes in the mean state that foster equatorial convection at the expense of that off the equator tend to decrease MJO amplitude in the model used here. These results are also consistent with the modeling results of *Hannah and Maloney* [2011], who showed that as GMS in the MJO convection region went up through parameterization changes, model MJO activity decreased. We also showed that reorganization of the large-scale circulation and changes in mean latent heat flux distribution may also contribute to shifts in the mean state and intraseasonal variability in the patterned warming runs.

[51] We stress here again that our results do not entail a prediction of how future MJO activity will change in the real climate. We begin our simulations with an aquaplanet SST distribution that is highly idealized and that does not resemble the real world in many important ways, although further experiments with a more realistic control SST distribution (but with less realistic MJO) produce the same conclusion that changes in future MJO activity are likely to be sensitive to the pattern of SST change. Also, the model physics in the version of CAM used here are admittedly imperfect, and it is conceivable that the results presented here would be different if the physical parameterizations were improved. Other CMIP models differ in their patterns of future warming from those of the CM2.1 model [*Zhao and Held*, 2012], and the SST pattern differences account for one third of intermodel variability in tropical precipitation change [*Ma and Xie*, 2013]. Experimentation with different warming patterns may help to better characterize the range of sensitivity of our results. Regardless, our results strongly suggest that when assessing changes in MJO activity in a future climate, we should pay heed to the future pattern of SST warming.

[52] **Acknowledgments.** We thank three reviewers for their comments that have significantly improved the manuscript. This work was supported by the Climate and Large-Scale Dynamics Program of the National Science Foundation under grants AGS-1062161, AGS-1025584 (EDM) and ATM-0854365 (SPX), and by the NOAA MAPP program under grants NA08OAR4320893 7 and 14 (EDM) and NA08OAR4320910 (SPX). The statements, findings, conclusions, and recommendations do not necessarily reflect the views of NSF, NOAA, or the Department of Commerce.

References

Allen, M. R., and W. J. Ingram (2002), Constraints on future changes in climate and the hydrologic cycle, *Nature*, *419*, 224–228.

Andersen, J. A., and Z. Kuang (2012), Moist static energy budget of MJO-like disturbances in the atmosphere of a zonally symmetric aquaplanet, *J. Clim.*, *25*, 2782–2804.

Back, L. E, and C. S. Bretherton (2006), Geographic variability in the export of moist static energy and vertical motion profiles in the Tropical Pacific, *Geophys. Res. Lett.*, *33*, L17810, doi:10.1029/2006GL026672.

Back, L. E., and C. S. Bretherton (2009), On the relationship between SST gradients, boundary layer winds, and convergence over the Tropical Oceans, *J. Clim.*, *22*, 4182–4196.

Benedict, J. J., A. H. Sobel, E. D. Maloney, D. M. Frierson, and L. J. Donner (2013), Tropical intraseasonal variability in Version 3 of the GFDL Atmosphere Model, *J. Climate*, in press.

Bony, S., M. Webb, C. Bretherton, S. Klein, P. Siebesma, G. Tselioudis, and M. Zhang (2011), CFMIP: Towards a better evaluation and understanding of clouds and cloud feedbacks in CMIP5 models, *CLIVAR Exch.*, *16*, 20–24.

Broccoli, A. J., K. A. Dahl, and R. J. Stouffer (2006), Response of the ITCZ to Northern Hemisphere cooling, *Geophys. Res. Lett.*, *33*, L01702, doi:10.1029/2005GL024546.

Cess, R. D., et al. (1990), Intercomparison and interpretation of cloud-climate feedback processes in 19 atmospheric general circulation models, *J. Geophys. Res.*, *95*, 16,601–16,615.

Charney, J. G. (1963), A note on large-scale motions in the tropics, *J. Atmos. Sci.*, *20*, 607–609.

Chou, C., J. D. Neelin, C.-A. Chen, and J.-Y. Tu (2009), Evaluating the "rich-get-richer" mechanism in tropical precipitation change under global warming, *J. Clim.*, *22*, 1982–2005.

Collins, W. D., et al. (2006), The formulation and simulation of the community atmosphere model: CAM3, *J. Clim.*, *19*, 2144–2161.

Delworth, T. L., et al. (2006), GFDL's CM2 global coupled climate models. Part I: Formulation and simulation characteristics, *J. Clim.*, *19*, 643–674.

Deser, C., and A. S. Phillips (2009), Atmospheric circulation trends, 1950–2000: The relative roles of sea surface temperature forcing and direct atmospheric radiative forcing, *J. Clim.*, *22*, 396–413.

Hannah, W. M., and E. D. Maloney (2011), The role of moisture-convection feedbacks in simulating the Madden-Julian oscillation, *J. Clim.*, *24*, 2754–2770.

Hendon, H. H., C. Zhang, and J. D. Glick (1999), Interannual variation of the Madden–Julian oscillation during austral summer, *J. Clim.*, *12*, 2538–2550.

Hendon, H. H., M. C. Wheeler, and C. Zhang (2007), Seasonal dependence of the MJO–ENSO relationship, *J. Clim.*, *20*, 531–543.

Inness, P. M., J. M. Slingo, E. Guilyardi, and J. Cole (2003), Simulation of the Madden–Julian oscillation in a coupled general circulation model. Part II: The role of the basic state, *J. Clim.*, *16*, 365–382.

Johnson, N. C., and S.-P. Xie (2010), Changes in the sea surface temperature threshold for tropical convection, *Nature Geosci.*, *3*, 842–845.

Jones, C., and L. M. V. Carvalho (2006), Changes in the activity of the Madden–Julian oscillation during 1958–2004, *J. Clim.*, *19*, 6353–6370.

Jones, C. and L. M. V. Carvalho (2010), Will global warming modify the activity of the Madden–Julian oscillation? *Q. J. R. Meteorol. Soc.*, *137*, 544–552.

Kang, S. M., I. M. Held, D. M. W. Frierson, and M. Zhao (2008), The response of the ITCZ to extratropical thermal forcing: Idealized slab-ocean experiments with a GCM, *J. Clim.*, *21*, 3521–3532.

Kiranmayi, L., and E. D. Maloney (2011), Effect of SST distribution and radiative feedbacks on the simulation of intraseasonal variability in an aquaplanet GCM, *J. Meteorol. Soc. Jpn.*, *89*, 195–210.

Knutson, T. R., and S. Manabe (1995), Time-mean response over the Tropical Pacific to increased CO_2 in a coupled ocean-atmosphere model, *J. Clim.*, *8*, 2181–2199.

Lindzen, R. S., and S. Nigam (1987), On the role of sea surface temperature gradients in forcing low-level winds and convergence in the tropics, *J. Atmos. Sci.*, *44*, 2418–2436.

Liu, P. (2013), Changes in a modeled MJO with idealized global warming, *Clim. Dyn.*, doi:10.1007/s00382-012-1323-2, in press.

Ma, J., and S.-P. Xie (2013), Regional patterns of sea surface temperature change: A source of uncertainty in future projections of precipitation and atmospheric circulation, *J. Clim.*, doi:10.1175/JCLI-D-12-00283.1, in press.

Maloney, E. D. (2009), The moist static energy budget of a composite tropical intraseasonal oscillation in a climate model, *J. Clim.*, *22*, 711–729.

Maloney, E. D., and D. L. Hartmann (2000), Modulation of eastern north Pacific hurricanes by the Madden-Julian oscillation, *J. Clim.*, *13*, 1451–1460.

Maloney, E. D., A. H. Sobel, and W. M. Hannah (2010), Intraseasonal variability in an aquaplanet general circulation model, *J. Adv. Model. Earth. Syst*, *2*, Art. 5, 24 pp., doi:10.3894/JAMES.2010.2.5.

McPhaden, M. J. (1999), Genesis and evolution of the 1997–98 El Niño, *Science*, *283*, 950–954, doi:10.1126/science.283.5404.950.

Molinari, J. and D. Vollaro (2000), Planetary- and synoptic-scale influences on Eastern Pacific tropical cyclogenesis, *Mon. Weather. Rev.*, *128*, 3296–3307.

Moore, A. M., and R. Kleeman (1999), Stochastic forcing of ENSO by the intraseasonal oscillation, *J. Clim.*, *12*, 1199–1220, doi:http://dx.doi.org/10.1175/1520-0442(1999)012<1199:SFOEBT>2.0.CO;2.

Moorthi, S., and M. J. Suarez (1992), Relaxed Arakawa-Schubert: A parameterization of moist convection for general circulation models, *Mon. Weather Rev.*, *120*, 978–1002.

Neale, R. B., J. H. Richter, and M. Jochum (2008), The impact of convection on ENSO: From a delayed oscillator to a series of events, *J. Clim.*, *21*, 5904–5924.

Neelin, J. D., and I. M. Held (1987), Modeling tropical convergence based on the moist static energy budget, *Mon. Weather Rev.*, *115*, 3–12.

Neelin, J. D., C. Chou, and H. Su (2003), Tropical drought regions in global warming and El Nino teleconnections, *Geophys. Res. Lett.*, *30*, 2275, doi:10.1029/2003GL018625.

Peters, M. E., Z. Kuang, and C. Walker (2008), Analysis of atmospheric energy transport in ERA40 and implications for simple models of the mean tropical circulation, *J. Clim.*, *21*, 5229–5241.

Pohl, B., and A. J. Matthews (2007), Observed changes in the lifetime and amplitude of the Madden–Julian oscillation associated with interannual ENSO sea surface temperature anomalies, *J. Clim.*, *20*, 2659–2674.

Randall, D. A., et al. (2007), Climate models and their evaluation, in *Climate Change 2007: The Physical Science Basis*, edited by S. Solomon, et al., pp. 589–662, Cambridge Univ. Press, Cambridge.

Raymond, D. J. (2001), A new model of the Madden–Julian oscillation, *J. Atmos. Sci.*, *58*, 2807–2819.

Raymond, D. J., and Ž. Fuchs (2009), Moisture modes and the Madden–Julian oscillation, *J. Clim.*, *22*, 3031–3046.

Raymond, D. J., S. L. Sessions, A. H. Sobel, and Z. Fuchs (2009), The mechanics of gross moist stability, *J. Adv. Model. Earth Syst.*, *1*, Art. 9, doi:10.3894/JAMES.2009.1.9.

Slingo, J. M., D. P. Rowell, K. R. Sperber, and F. Nortley (1999), On the predictability of the interannual behaviour of the Madden-Julian oscillation and its relationship with El Nino, *Q. J. R. Meteorol. Soc.*, *125*, 583–609.

Sobel, A. H., and C. S. Bretherton (2000), Modeling tropical precipitation in a single column, *J. Clim.*, *13*, 4378–4392.

Stevens, B., J. Duan, J. C. McWilliams, M. Münnich, and J. D. Neelin (2002), Entrainment, Rayleigh friction, and boundary layer winds over the tropical Pacific, *J. Clim.*, *15*, 30–44.

Takahashi, C., N. Sato, A. Seiki, K. Yoneyama, and R. Shirooka (2011), Projected future change of MJO and its extratropical teleconnection in East Asia during the northern winter simulated in IPCC AR4 models, *SOLA*, *7*, 201–204.

Tokioka, T., K. Yamazaki, A. Kitoh, and T. Ose (1988), The equatorial 30–60 day oscillation and the Arakawa–Schubert penetrative cumulus parameterization, *J. Meteorol. Soc. Jpn.*, *66*, 883–901.

Vecchi, G. A., and B. J. Soden (2007), Global warming and the weakening of the tropical circulation, *J. Clim.*, *20*, 4316–4340.

Wheeler, M., and G. N. Kiladis (1999), Convectively coupled equatorial waves: Analysis of clouds and temperature in the wavenumber-frequency domain, *J. Atmos. Sci.*, *56*, 374–399.

Xie, S.-P., C. Deser, G.A. Vecchi, J. Ma, H. Teng, and A.T. Wittenberg (2010), Global warming pattern formation: Sea surface temperature and rainfall, *J. Clim.*, *23*, 966–986.

Yoo, C., S. Feldstein, and S. Lee (2011), The impact of the Madden-Julian oscillation trend on the Arctic amplification of surface air temperature during the 1979–2008 boreal winter, *Geophys. Res. Lett.*, *38*, L24804, doi:10.1029/2011GL049881.

Zhao, M., and I. M. Held (2012), TC-permitting GCM simulations of hurricane frequency response to sea surface temperature anomalies projected for the late 21st century. *J. Clim.*, *25*, 2995–3009.

Corresponding author: E. D. Maloney, Department of Atmospheric Science, Colorado State University, 1371 Campus Delivery, Fort Collins, CO 80523-1371, USA. (emaloney@atmos.colostate.edu)